2

X-811-72-392

PREPRINT

NASA TM X- 66223

ANALYSIS OF A DUAL-REFLECTOR ANTENNA SYSTEM USING PHYSICAL OPTICS AND DIGITAL COMPUTERS

RICHARD F. SCHMIDT

(NASA-TM-X-66223) ANALYSIS OF A DUAL-REFLECTOR ANTENNA SYSTEM USING PHYSICAL OPTICS AND DIGITAL COMPUTERS (NASA) 42 p HC $4.25 CSCL 17B

N73-21183

Unclas

G3/07 69009

OCTOBER 1972

GSFC

GODDARD SPACE FLIGHT CENTER
GREENBELT, MARYLAND

42

X-811-72-392

AN ANALYSIS OF A DUAL-REFLECTOR ANTENNA SYSTEM USING PHYSICAL OPTICS AND DIGITAL COMPUTERS

Richard F. Schmidt

October 1972

Goddard Space Flight Center
Greenbelt, Maryland

AN ANALYSIS OF A DUAL-REFLECTOR ANTENNA SYSTEM USING PHYSICAL OPTICS AND DIGITAL COMPUTERS

Richard F. Schmidt
Network Engineering Division

ABSTRACT

This document discusses the application of physical-optics diffraction theory to a deployable dual-reflector geometry selected for study by the Jet Propulsion Laboratory, California Institute of Technology, Pasadena, California. The methods employed herein are not restricted to the "Conical-Gregorian" antenna, but apply in a general way to dual and even multiple reflector systems. Complex-vector wave methods are used in the Fresnel and Fraunhofer regions of the reflectors. Field amplitude, phase, polarization data, and time-average Poynting vectors are obtained via an IBM 360/91 digital computer. Focal-region characteristics are plotted with the aid of a CALCOMP plotter. Comparison between the GSFC Huygens-wavelet approach, JPL measurements, and JPL computer results based on the near-field spherical wave expansion method are made where-ever possible.

CONTENTS

ILLUSTRATIONS

GLOSSARY OF NOTATION

Symbol	Meaning
γ_i	the i^{th} surface when tracing rays or waves
F	focal length of the paraboloid
σ_{max}	maximum radius
σ_0	minimum radius
α	inclination angle of a parabolic arc
c	inverse slope of a cone
z_1	displacement of cone apex from origin
λ	wavelength
f	frequency
R_c	Rayleigh far-field criterion
d, D	diameter
$\mathfrak{F}$	feed function
r, θ, ϕ	observer coordinates radius, theta, phi
ρ, Θ, Φ	coordinates used with feed functions
N	exponent in feed function (pos., zero, or neg.)
$\overline{E}$, $\overline{H}$	electric and magnetic vector fields
x', y', z'	observer position in Cartesian coordinates
x, y, z	surface coordinates
$\overline{n}_i$	vector unit normal to surface
∇	del operator
ω	angular frequency
Ψ	solution to wave equation
μ, ϵ, σ	constitutive parameters: magnetic permeability, inductive capacity, electric conductivity
ds	differential area
k	wave number

$\hat{1}_r$, $\hat{1}_\theta$, $\hat{1}_\phi$	radial and transverse basis vectors (spherical)
$\bar{o}$	vector to surface from origin (x, y, z)
LI	integration sampling interval
$\bar{\rho}_\epsilon$	displacement vector for feeds, $(x_\epsilon, y_\epsilon, z_\epsilon)$
$\langle\bar{P}\rangle$	time-average Poynting vector
Re	real part of a complex quantity
$\hat{1}_x$, $\hat{1}_y$, $\hat{1}_z$	Cartesian basis vectors
s	width of a ray bundle
MP, CP	main polarization, cross polarization components
Ψ_{E_θ}	phase of electric field
P	magnitude of $\langle\bar{P}\rangle$
L_0	maximum plotted length of $\langle\bar{P}\rangle$
P_{min}, P_{max}	minimum and maximum values of $\langle\bar{P}\rangle$ on a decibel scale
E_r, E_θ, E_ϕ	spherical components of electric-field
E_x, E_y, E_z	Cartesian components of electric-field
*	complex conjugate
σ, ζ	radial and angular variables (cylindrical net)
∂	partial derivative
S_i	i th singularity
z_σ	partial derivative of z with respect to σ
ρ_σ, ρ_ζ	partial derivative of ρ with respect to σ, ζ

AN ANALYSIS OF A DUAL-REFLECTOR ANTENNA SYSTEM USING PHYSICAL OPTICS AND DIGITAL COMPUTERS

INTRODUCTION

The purpose of this document is (1) to provide a written record of a GSFC analysis of dual and multiple reflector systems, (2) discuss some aspects of the Conical-Gregorian arrangement, and (3) make a comparison between the GSFC Huygens-wavelet approach, JPL measurements, and JPL near-field spherical-wave expansion methods. Data accumulated by JPL for the Conical-Gregorian antenna is not reproduced here.[1]

The geometry of the system is shown as Fig. 1, together with the input parameters. It should be noted that a part of the conical main reflector is not illuminated under ray optics. An illumination function $\mathfrak{J} = \cos^N \Theta$, $N = 12.3750$ was used in the GSFC studies to achieve an edge taper of -18.0 db on the subreflector edge. Under ray optics the -18.0 db taper maps to the interior of the cone rather than the edge. A parametric representation is used for both surfaces, and can be found in the Appendix with other details of the computation.

FORMULATION OF THE SCATTERED FIELDS

Consider the formulation for the scattered fields (under transmission) and allow that every point of the conical main reflector is deep inside of the Fresnel region of the subreflector. Assume, further, that the observer of the fields of the main reflector may lie in either the Fresnel or Fraunhofer regions of the latter.

The fields due to the main reflector are computed via a formulation which is equivalent to Kirchhoff-Kottler and Franz formulations.[2]

---

[1] Ref 1, page 146

[2] Ref. 2, Chapter 8, pp. 460-470
Ref. 3, Chapter 5, pp. 158-162
Ref. 4 pp. 141-144
Ref. 5, pp. 114-115
Ref. 6, pp. 500-506

γ_1
$F = 2.47058'$
$\sigma_{max} = 1.40108'$
$\sigma_0 = 0.0'$
$\alpha = 50.0^\circ$ = inclination angle for parabolic arc

γ_2
$C = -0.46631$
$\sigma_{max} = 3.0'$
$\sigma_0 = 1.16667'$
$Z_1 = 0.90841'$

$\lambda = 0.11709'$
$f = 8.4$ GHz
$R_c = \frac{2d^2}{\lambda} = 134'$ for γ_1
based on physical aperture

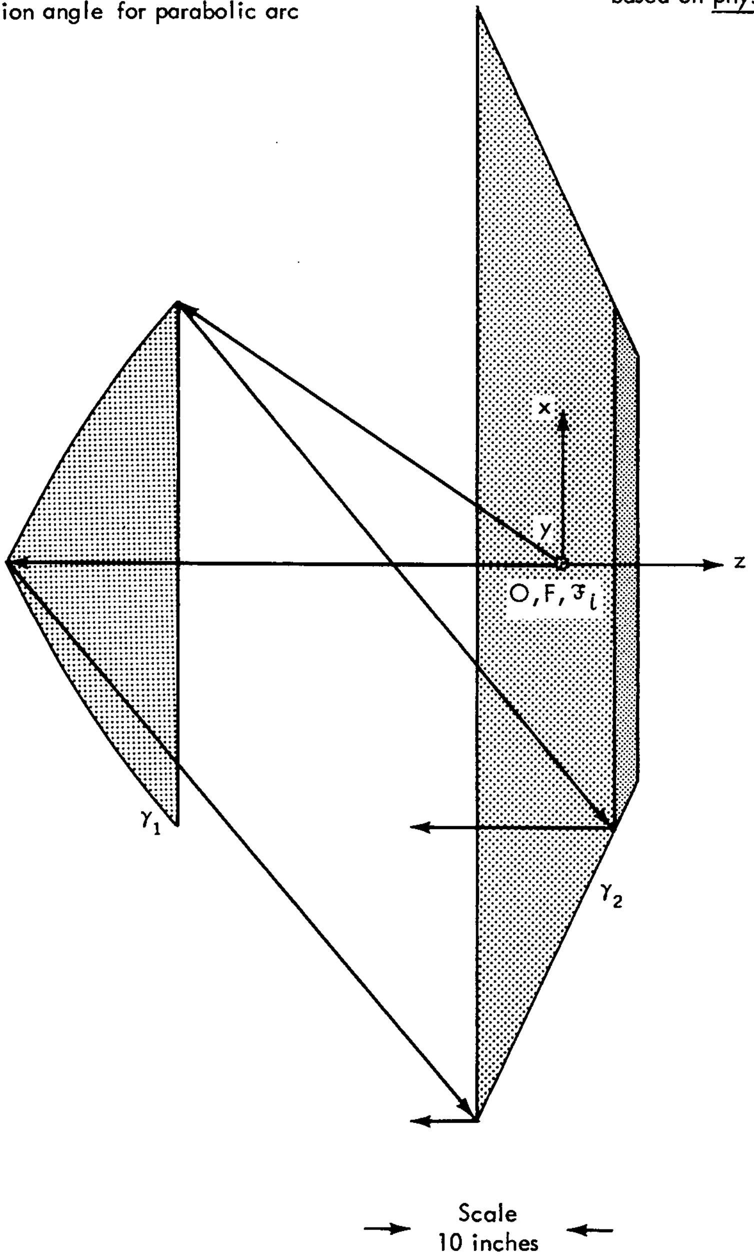

Figure 1. JPL Conical-Gregorian System

$$\bar{E}(x', y', z') = \frac{1}{j\,\omega\,\epsilon}\,\frac{1}{4\,\pi}\int_{\gamma_2}[(\bar{n}\times\bar{H}_2)\cdot\nabla]\,\nabla\Psi\,ds - j\,\omega\mu\,\frac{1}{4\,\pi}\int_{\gamma_2}(\bar{n}_2\times\bar{H}_2)\,\Psi\,ds,$$

$$\bar{H}(x', y', z') = -\frac{1}{4\,\pi}\int_{\gamma_2}(\bar{n}_2\times\bar{H}_2)\times\nabla\Psi\,ds,$$

where

$$\Psi = \frac{e^{-jkr}}{r}$$

and

$$\nabla\Psi = -\left(j\,k + \frac{1}{r}\right)\Psi\,\hat{1}_r$$

taking $\hat{1}_r$ in a local context on the reflecting surface.

Since only the magnetic field $\bar{H}_2$ is required on γ_2 , the integral

$$\bar{H}_2(x_2', y_2', z_2') = -\frac{1}{4\,\pi}\int_{\gamma_1}(\bar{n}_1\times\bar{H}_1)\times\nabla\Psi\,ds$$

over γ_1 is sufficient to obtain the illumination of the conical reflector.

Some studies on the subsystem were performed in the Fresnel and Fraunhofer regions. A separate program was used in this instance to evaluate

$$\bar{E}(x', y', z') = \frac{1}{j\,\omega\,\epsilon}\,\frac{1}{4\,\pi}\int_{\gamma_1}[(\bar{n}_1\times\bar{H}_1)\cdot\nabla]\,\nabla\Psi\,ds - j\,\omega\,\mu\,\frac{1}{4\,\pi}\int_{\gamma_1}(\bar{n}_1\times\bar{H}_1)\,\nabla\Psi\,dS_S$$

and

$$\bar{H}(x', y', z') = -\frac{1}{4\,\pi}\int_{\gamma_1}(\bar{n}_1\times\bar{H}_1)\times\nabla\Psi\,ds$$

It is noted that every value $\bar{H}_2$ on γ_2 is obtained by summing the Huygens wavelets over all of γ_1 (an m:1 mapping) which is distinct from ray optics (a 1:1 mapping). Scattered fields under reception are obtained in the same manner as those under transmission, however, the conical reflector is now γ_1 and the subreflector is now γ_2. With this interchange, the preceding integrals for $\bar{E}(x', y', z')$ and $\bar{H}(x', y', z')$ in the focal region can be formed by the same logical process.

THE SUBSYSTEM

On occasion it is helpful to study a subsystem to effect design changes, obtain better insight with regard to the electromagnetic fields and wavefronts, or to verify satisfactory performance and avoid programming errors in a multi-reflector system. The results of the GSFC far-field computations for the subreflector are given in Fig. 2 and 3. These agree quite closely with the measured and calculated data (not reproduced here). The central spike at $\theta = 0°$ is observed and is about 17 db below the peak at $\theta = 50°$ (the inclination angle α_p of the parabolic arc). The single cut provided by the JPL article shows a central spike about 18 db below the peak at approximately $\theta = 50°$, reading the graphical results. Feed displacement ($\bar{\rho}_\epsilon$) equals zero here.

Although good agreement was obtained when comparing the far-field subreflector patterns of two independent simulations and a measurement, these patterns do not impinge on the conical main reflector. For this reason, JPL utilizes the near-field spherical wave expansion method. In the GSFC approach the Huygens wavelet approach is retained, but consideration is given to the near-field geometry in summing the wavelets. Actually, it would appear that the time-average Pounting vector provides a more comprehensive measure of the electromagnetic effects in a Fresnel region than either the electric or magnetic fields. The basis of this viewpoint is the fact that power flow is affected when fields are asynchronous in time and non-orthogonal in space. The time-average Poynting vector incorporates all of these effects, to whatever degree they may be present, since

$$\langle \bar{P} \rangle = \frac{1}{2} \mathrm{Re}\, \bar{E} \times \bar{H}^*$$

is sensitive to spatial orientation of the fields and the relative phase between electric and magnetic fields. This product is also sensitive to the magnitude of each of the fields, which may be especially important if the electric and magnetic fields in a near-field or intermediate near-field region are not related simply, as in a far-field region.

Plots of the time-average Poynting vector passing through the aperture plane of the conical main reflector are given as Fig. 4 and Fig. 5. It can be seen that the power density of the central spike is of the same order of magnitude as the intensity at $\theta = 50°$, which is distinct from the 18 db difference shown by the far-field pattern discussed previously. Solid lines in Fig. 4 and Fig. 5 indicate the intersection of the geometrical bounds with the aperture plane.

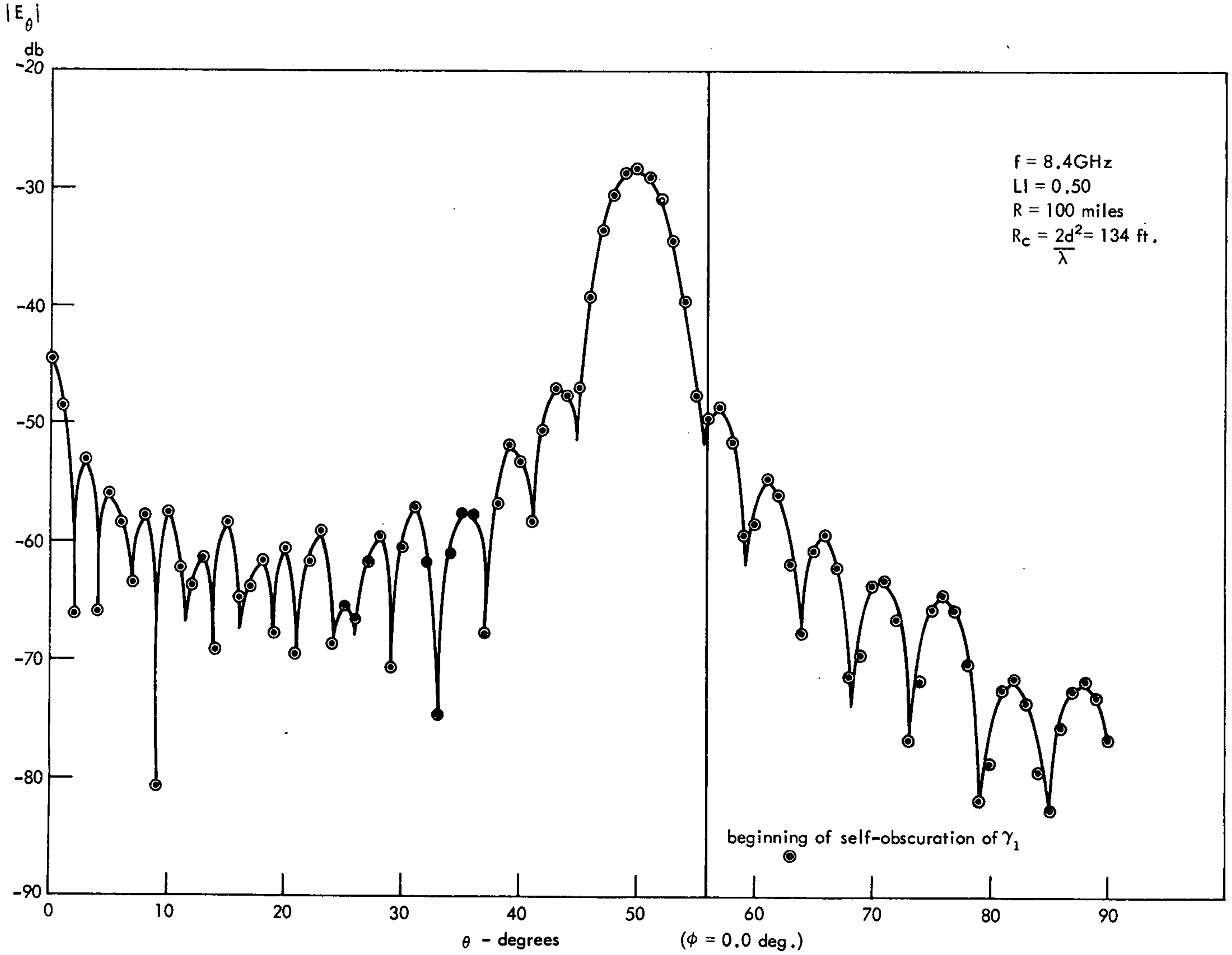

Figure 2. Fraunhofer Pattern E_θ due to subreflector (ϕ=0.0 °)

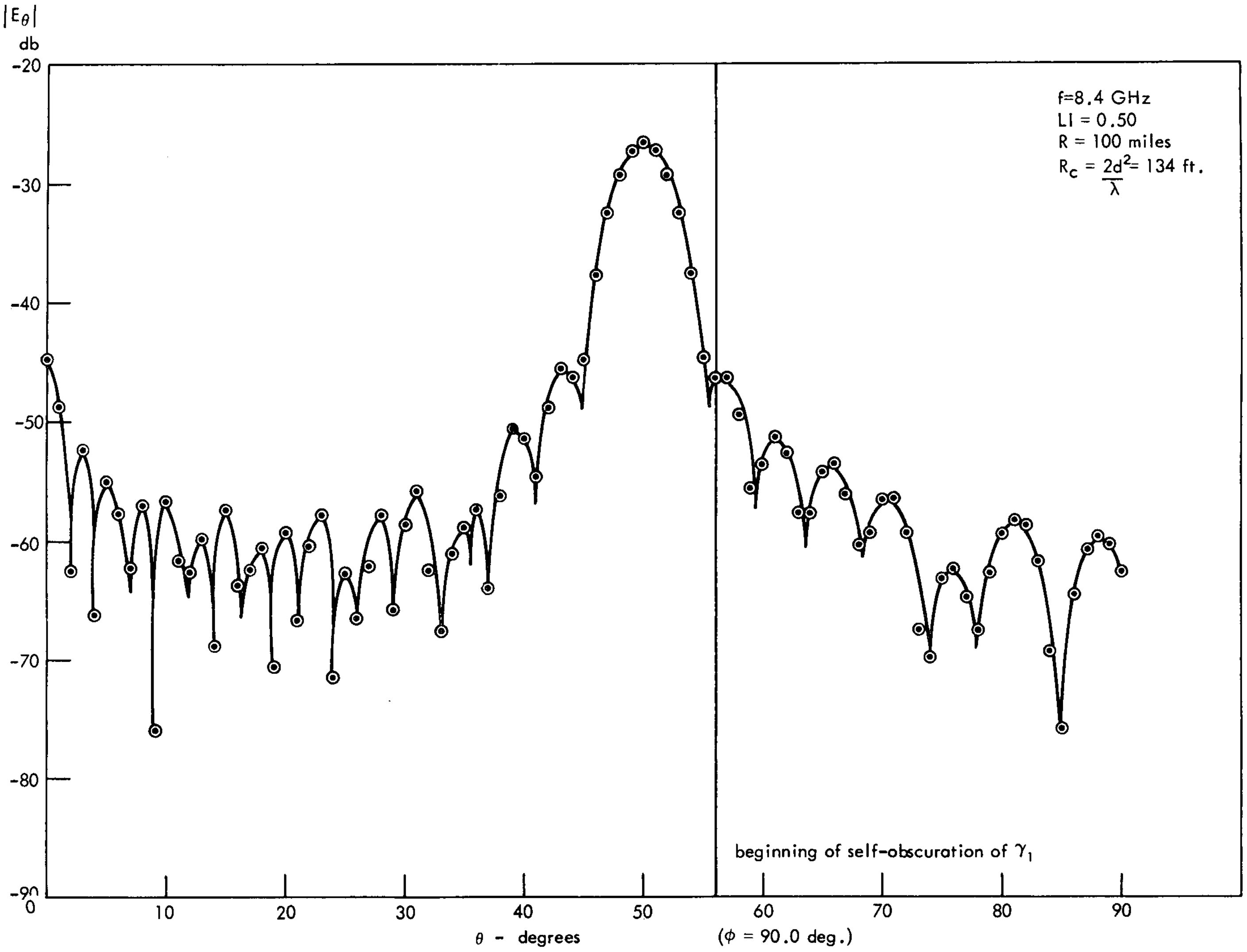

Figure 3. Fraunhofer Pattern E_θ due to subreflector ($\phi = 90.0°$)

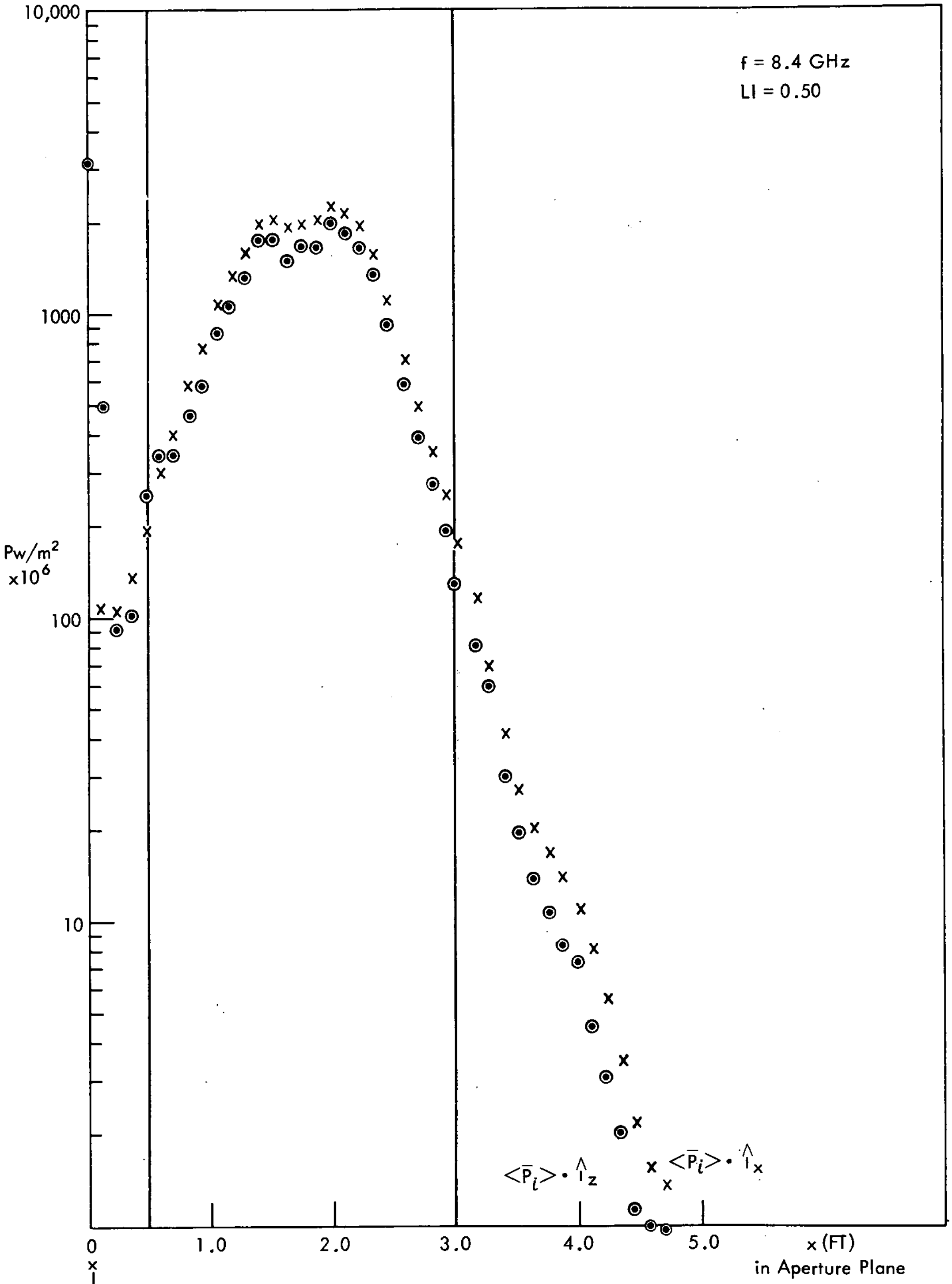

Figure 4. Components of $\langle\bar{P}\rangle$ in aperture plane (x-direction)

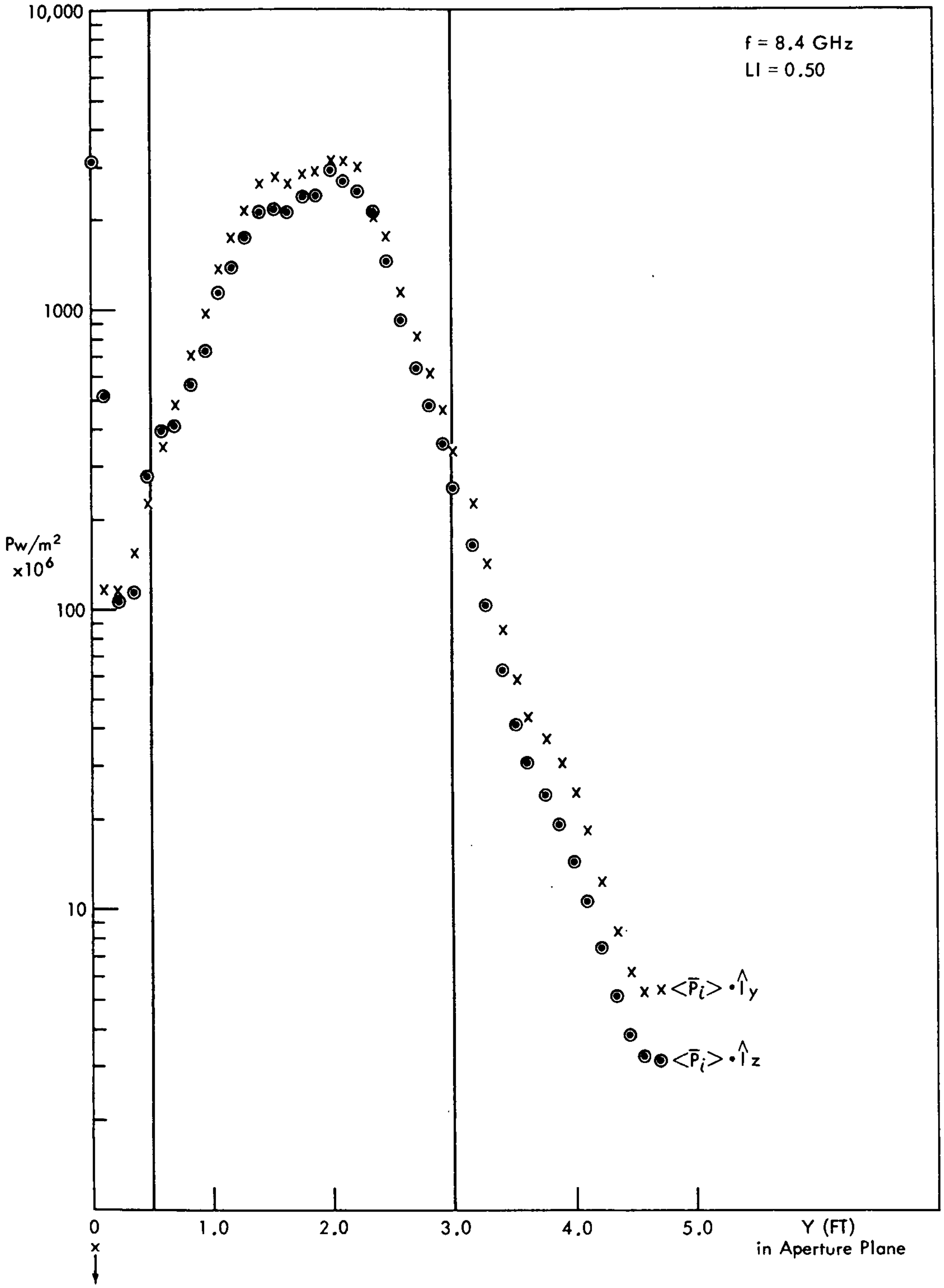

Figure 5. Components of ⟨ $\overline{P}$ ⟩ in aperture plane (y direction)

Detailed studies of the subsystem were made by exploring areas of the incident ray bundle from the subreflector in the vicinity of the conical main reflector. These were Fresnel region studies of field amplitude, phase, and the time-average Poynting vectors for both scanned and unscanned transmission modes. The plots are highly detailed and not presented here. In general they established the following. The near-field analysis agrees quite closely with the ray-optics predictions in most respects – wavefronts are orthogonal to rays from the subreflector, and time-average Poynting vector plots show power-flow along the rays. It is noted, however, that the diffraction analysis shows details not provided by ray-optics. Rays carry with them no accurate measure of intensity, whereas the Poynting vectors were significantly reduced near the edges of ray bundles, etc. The power flow for both scanned and unscanned cases, as well as the wave fronts, were exceptionally orderly or homogeneous.

In contrast to this, the electric fields due to the subreflector showed interesting characteristics. Constant-intensity plots yielded a lamellar-type set of contours in the central portion of the ray bundles. This can be attributed to the prime-feed weighting of the subreflector illumination distribution, modified by the effects of phase stationarity in the Fresnel region. The computed divergence of electric field intensity via diffraction was found to agree closely with the law or rule of divergence that can be inferred from energy conservation principles.

Since the rays due to the subreflector pass orthogonally through the slant surface of a truncated imaginary cone, and since total far-field radiated energy is invariant, it follows that

$$E \alpha [\pi (2 r \tan \alpha_p - s \cos \alpha_p]^{-1/2}$$

When range r from the subreflector is large, the above reduces to

$$E \alpha \frac{1}{\sqrt{r}}$$

which is the same as the law of divergence for cylindrical waves. In the preceding, (s) is the width of the ray bundle in Fig. 1, and the slant height of the imaginary cone. As before, α_p is the inclination angle of the parabolic arc used to generate the subreflector surface. The expression has significance for values of r such that the power flows through a cone or a truncated cone.

THE DUAL REFLECTOR SYSTEM

The backscattered radiation patterns of the dual-reflector system were computed using the previously cited parameters to determine the agreement with JPL measured data and the near-field spherical-wave expansion method. The GSFC approach depends entirely on Huygens wavelets. Previous discussion pointed out that the illumination on the subreflector, obtained here by a directive point-source feed function is a one-to-one (1:1) mapping. The illumination on the main reflector is by contrast, a many-to-one (m:1) mapping over γ_1. Fresnel or Fraunhofer fields due to γ_2 are likewise obtained as a many-to-one mapping (n:1) taken over γ_2. This should be contrasted with ray-optics analyses.

Three sets of integration sampling intervals were chosen for the main and subreflector surfaces. These were $LI_2 = 3.0$, $LI_1 = 1.0$; $LI_2 = 1.5$, $LI_1 = 1.0$; $LI_2 = 1.5$, $LI_1 = 0.5$ respectively, in wavelengths. An analogue to Shannon's sampling theorem indicates that curvilinear quadrilaterals on antenna surfaces should not exceed 0.5 λ on an edge, however, it has been found advantageous to explore intervals both larger and smaller to obtain a satisfactory compromise or trade-off between accuracy and economy. Planar "cuts" at $\phi = 0°$, 45°, and 90° were taken for each set of LI specified, above, to establish the stability of the solutions with respect to LI. It was found that cpu time was approximately 3/4 minute, 1 minute, and 3 minutes for the sampling criteria employed here. These cpu times should be assessed after recalling that significant deviations among the patterns occurred in the vicinity of the third side lobe and beyond.

Figure 6 corresponds to the cut $\phi = 0.0°$, obtained with $LI_2 = 1.5$, $LI_1 = 0.5$, and is an E-plane cut showing both the magnitude of the electric field $|E_\theta|$, and the associated phase $\Psi_{E\theta}$. It was found that cross-polarization components for principal-plane cuts were 80 db to 100 db below beam peaks and are,therefore, not presented here. In the diagonal or $\phi = 45°$ cuts cross-polarization was about 25 db below beam peaks, and the form of the pattern was the characteristic vee-shaped cross-polarization pattern that is obtained with single-reflector systems (paraboloids, for example). H-plane and diagonal cuts were very similar to the E-plane cut, and are not presented here.

An appreciation of the effect of sampling can be obtained from Fig. 7, which also shows JPL measured and calculated results superimposed on GSFC data for the $\phi = 0°$ pattern cut. Side-lobe levels are presented as a function of integration sampling intervals (LI) up to, and including, the fifth sidelobe. It is noted that the convergence to the solution is oscillatory and not monotonic with respect to sampling (LI). JPL measured data is double-valued for a given sidelobe in some instances and this is probably attributable to surface fabrication errors, system asymmetries, and slight pattern-range variations. In any event, the largest measured deviation is 3 db, occurring at a level of 26 db below the beam-maximum level.

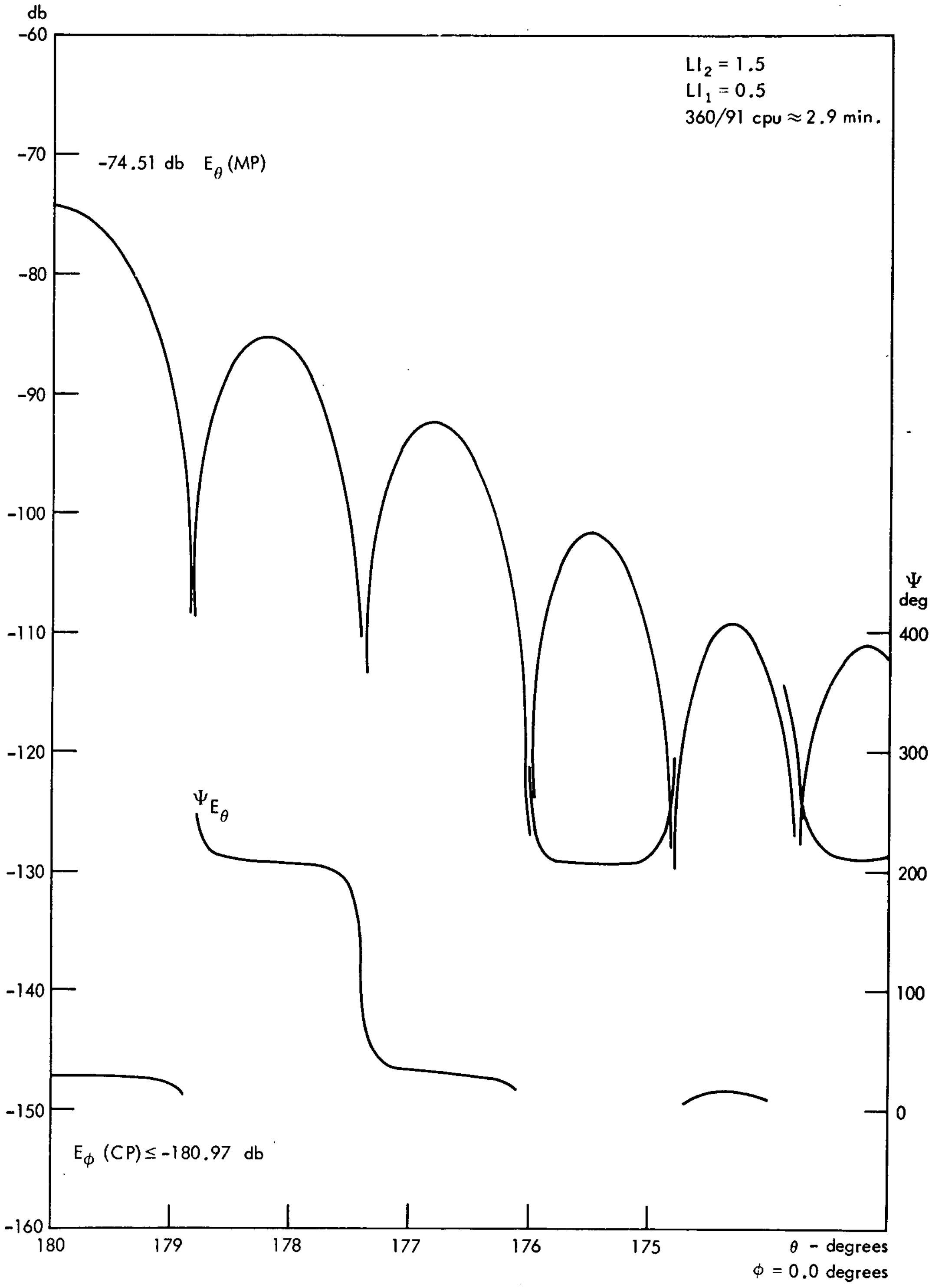

Figure 6. Fraunhofer patterns E_θ, Ψ_{E_θ} of Conical-Gregorian system ($\phi = 0.0°$)

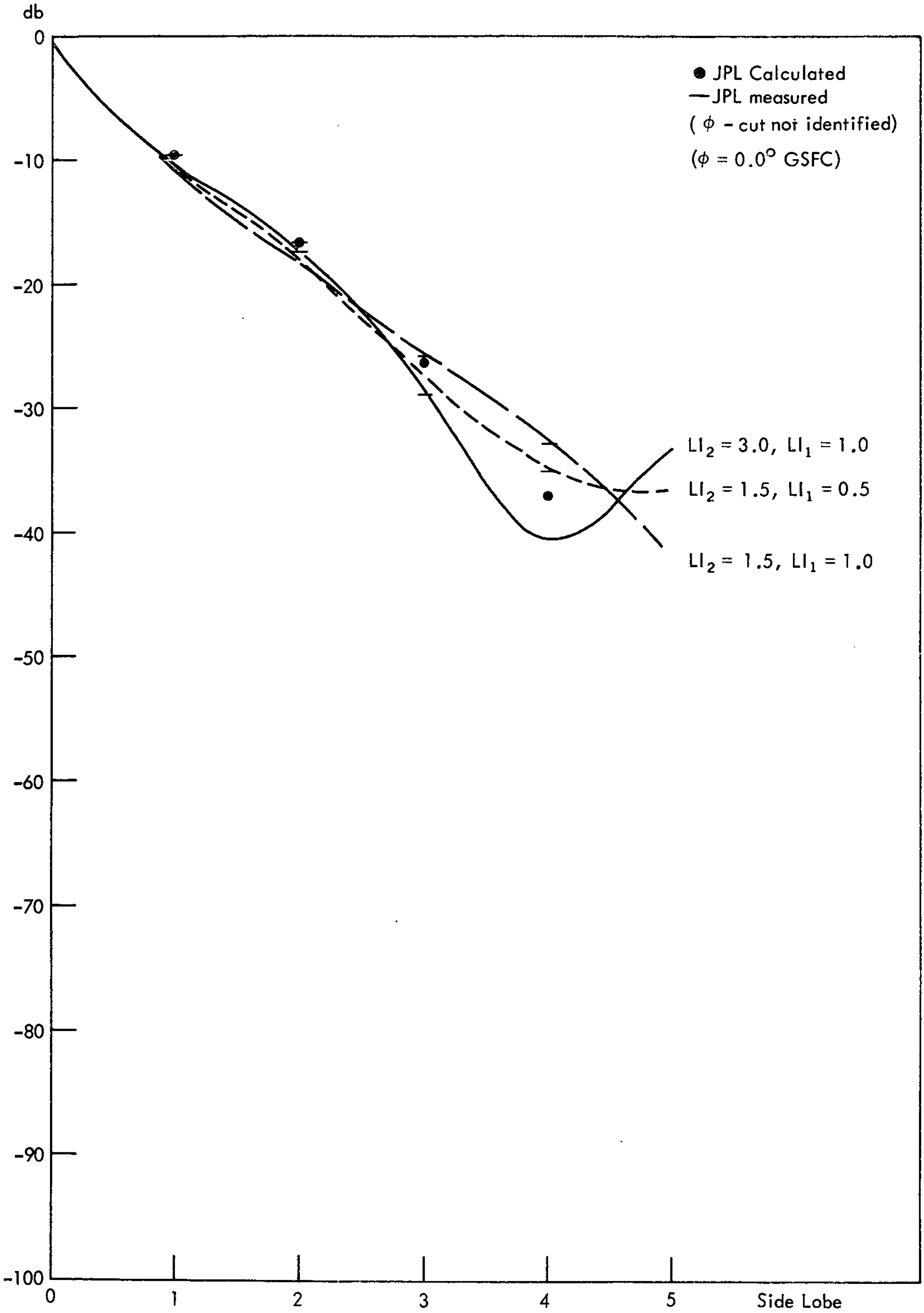

Figure 7. Side-lobe levels versus integration sampling intervals

A very brief study pertaining to the stationarity of the phase of the waves arriving at the main reflector aperture plane was made using $LI_2 = 3.0$ and $LI_1 = 1.0$. It should be recalled that the JPL conical main reflector, Fig. 1, extended beyond the geometrical interior bound from $\sigma_{02} = 1.40$ ft to $\sigma_{02} = 1.17$ to enhance the system directive gain. By ray optics there is no access to the shaded portion of the conical main reflector (i.e. no illumination from the subreflector), but all wavelets from γ_1 have access to every point on γ_2. The following Table sums-up the findings when $LI_2 = 3.0$ and $LI_1 = 1.0$.

Inner Radius of Conical Main Reflector (ft.)		Electric Field $\lvert E_\theta \rvert$ (db scale)
2.00		-76.84
1.75		-75.38
1.50		-74.63
1.40	$\sigma_{02} = \sigma_{m1}$ (JPL value)	-74.77
1.17		-74.56
1.00		-74.93
0.75		-74.84
0.50		-75.05
0.00		-74.94

The large increase in area on γ_2, exceeding the JPL design area by about 23 percent when $\sigma_{02} = 0.0$, results in a decrease in on-axis intensity of about 0.38 db due to a lack of stationarity. Of the values of σ_{02} used, none lead to an intensity exceeding that obtained with the JPL value $\sigma_{02} = 1.17$ ft. (approx.). The sharp reduction in gain for $\sigma_{02} > 1.40$ ft is due to the removal of cophased or stationary aperture distribution.

A brief study of the beam scanning characteristics of the Conical-Gregorian antenna indicated that beam squint-angle (θ_s) varied almost linearly from 0.0° to 0.84° as feed displacement (x_ϵ) in the xy feed plane varied from $0.0\ \lambda$ to $1.5\ \lambda$. Comma-lobe levels about 7.2 db below beam peaks were observed, for a series of computations carried out at the three sets of sampling criteria employed earlier for unscanned beams, at the limit of scan $\theta_s = 0.84°$.

The next step, after beam-scanning of individual beams, was to use four feeds in a conventional amplitude-sensing monopulse configuration. Feeds were displaced $\lambda/4$ in both x and y directions for $z = 0$, the feed plane, in an initial computation to recover the monopulse sum and difference patterns of this dual-reflector system. The resulting sum and difference patterns of Fig. 8 and 9, taken at $\phi = 0.0°$, are representative of the results. Other cuts, obtained at $\phi = 45.0°$ and $\phi = 90.0°$ for both telemetry and error channels are not reproduced

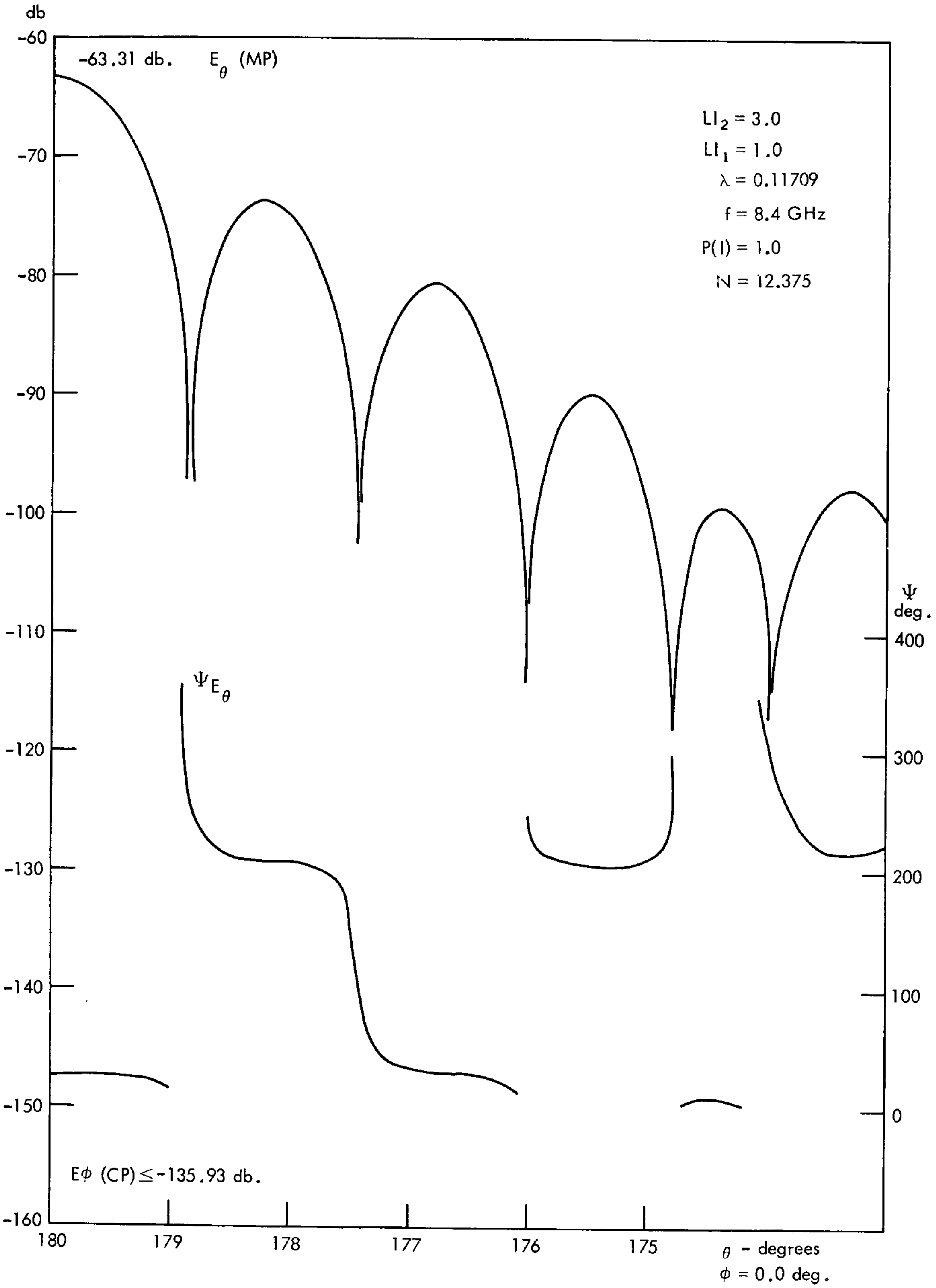

Figure 8. Monpulse sum pattern

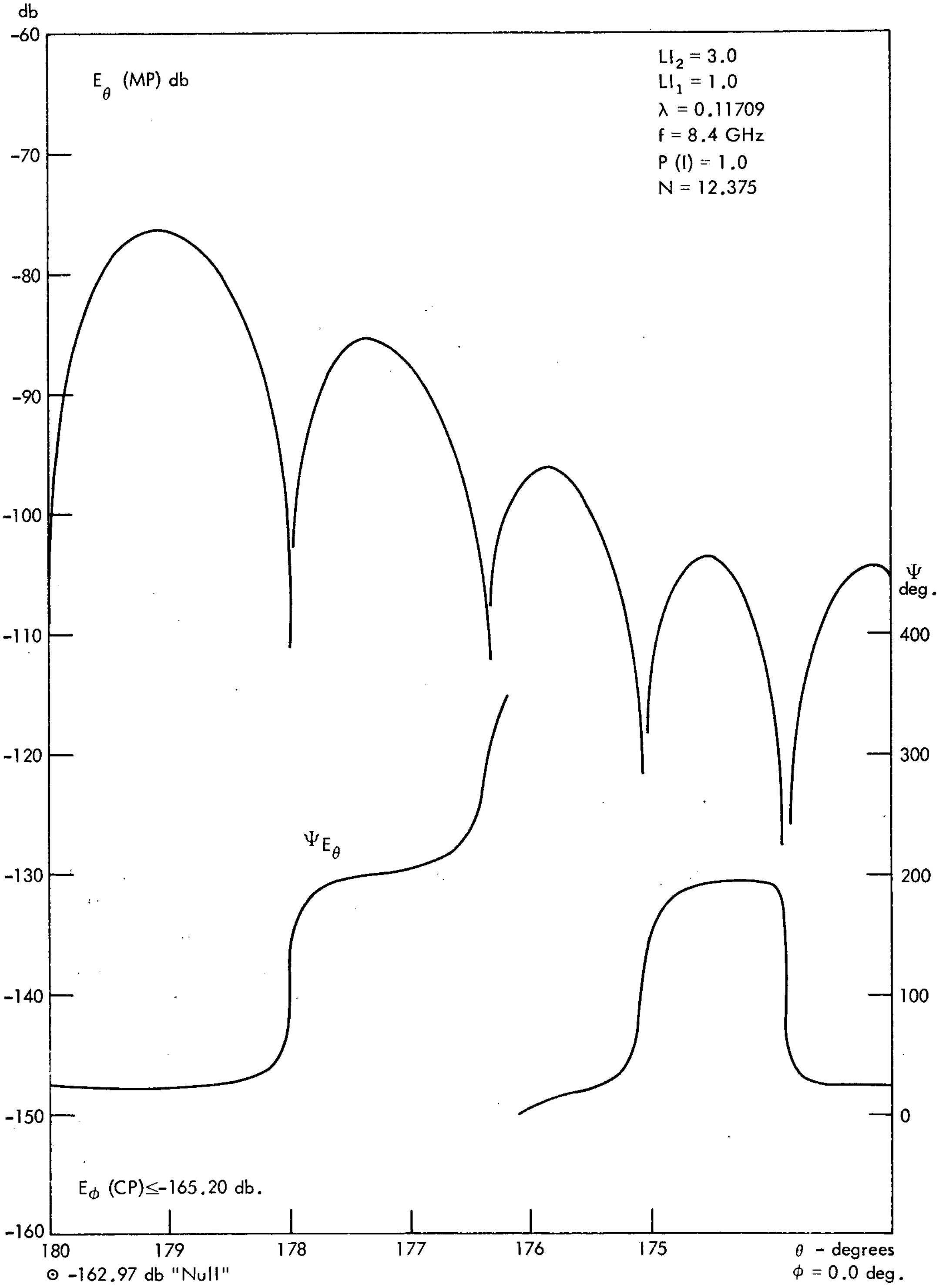

Figure 9. Monpulse difference pattern

here. Sum channel sidelobes as high as 9.0 decibels below the axial peak value were noted. Cross-polarization in the $\phi = 45.0°$ cuts reached 26.0 db below axial peak level for the sum channel. Error channel cross-polarization levels were about 40.0 db below the axial peak level of the sum channel.

Since the dual-reflector system studied here has a magnification factor similar to that of a conventional Cassegrain, the feeds were displaced $\lambda/2$ in both x and y directions for $z = 0$. Results were very similar to the case of $\lambda/4$ feed displacement, although sum-channel gain was reduced by about 2.3 db. The error channel slope was not noticeably affected. It appears that a better selection of monopulse feeds could be made by means of a careful examination of the feed directivity for a given geometry, increasing the number of feeds to produce a larger "effective" area (increasing the number of feeds to 16 for example), and by a mapping of the Airy disc and ring structure under reception to determine the size of the focal region. The mapping of the focal region in two transverse planes was carried out for the Conical-Gregorian antenna and is discussed in the last section of this report.

Numerous other studies were either made in detail, or planned, as they were within the capability of the program. Some of these are "squinted" monopulse, variation of feed directivity, and studies of system sensitivity with respect to the axial and lateral placement of the feeds and the reflector elements. These are not presented here as they are straightforward applications of the program and are not of general interest.

FOCAL-REGION MAPPING

Focal-region mapping[1] was restricted to the case of axial plane-wave reception. The simulation approximated the latter by means of an isotropic source (in amplitude) polarized in the "vertical" sense, P(I) = 1.0 polarization moment, and situated 100 miles from the origin of coordinates (the feed point of the system). Under reception, the plane wave of the simulation impinges on the conical main reflector (γ_1), and is converged to the subreflector (γ_2) where the final convergence is to the focal region. See Fig. 10. Ordinarily the Airy disc and ring structure is of interest, as is the depth of field of the system. These can be found by searching for, or computing, fields in the xy and yz planes, respectively, for the polarization selected here. It is anticipated that the Airy disc, whose radius is given by[2]

---

[1] Ref. 7, pp. 777-783
Ref. 8, pp. 935-943

[2] Ref. 9, p. 283

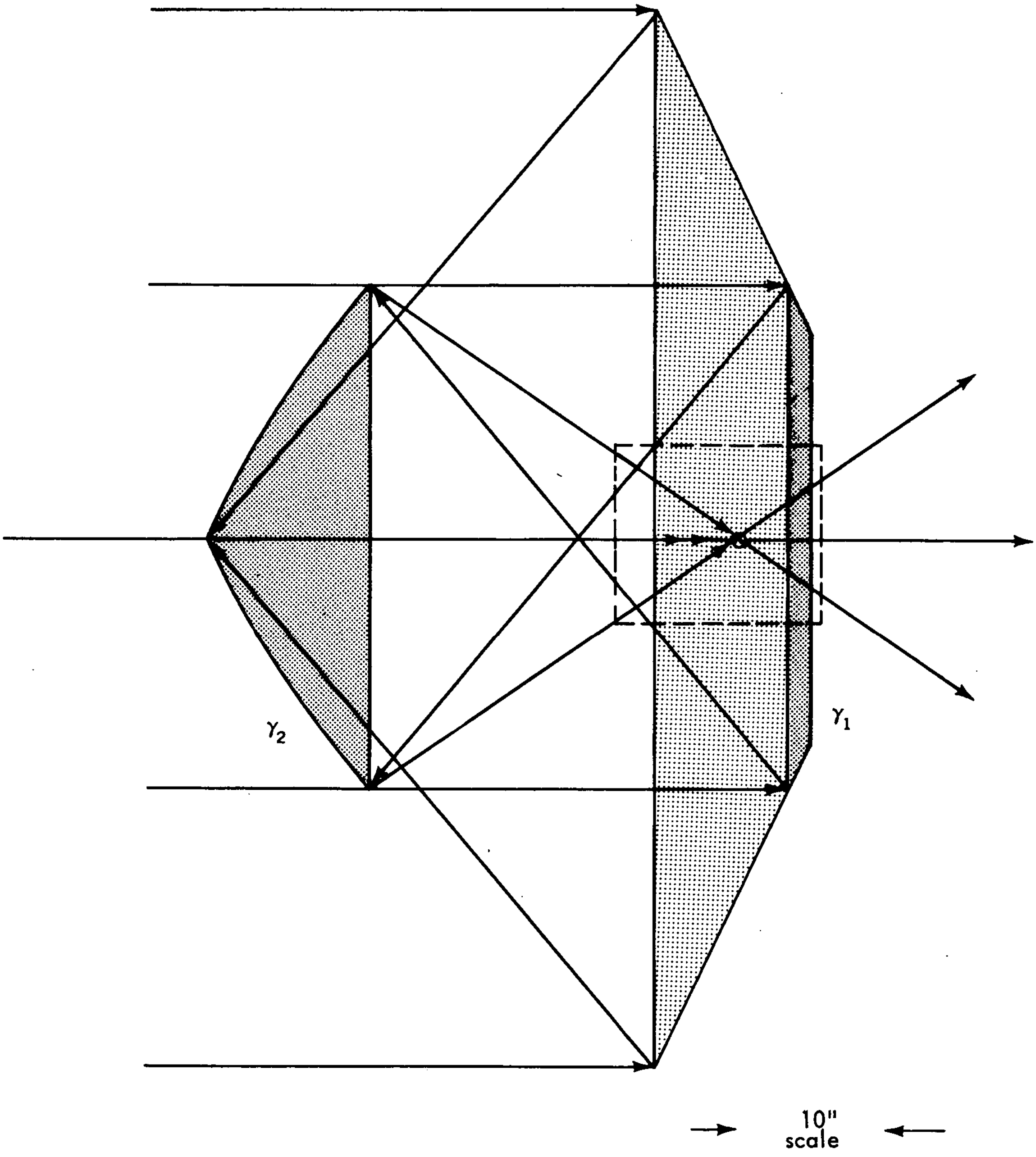

Figure 10. Ray-trace for reception

$$R_{AD} = 1.22 \frac{F\lambda}{D}$$

for parabolic reflectors, should be broadened due to the magnification factor of the Conical-Gregorian system. Likewise the depth of field should be extended.

The "Airy disc" structure was obtained on the assumption that convergence would be in the feed-plane of the system. Only the electric field E_x was plotted to illustrate the disc and ring structure of the focal region using polarization moment P(I) = 1.0 for the incident plane-wave. The results are shown as Fig. 11 and Fig. 12 with nulls and a few quantitative values retained. These contours were obtained from a field of values at a resolution of $\lambda/10$ with $LI_1 = 3.0$, $LI_2 = 1.0$ and $LI_1 = 1.5$, $LI_2 = 0.5$. Inadequate sampling is depicted by Fig. 11. A third computer run, not illustrated, at a sampling interval $LI_1 = 1.0$ for the conical main reflector and $LI_2 = 0.5$ for the JPL subreflector, established the fact that the results of Fig. 12 were stable with respect to the integration interval.

In order to present a graphic illustration of the behavior of the focal-region for the Conical Gregorian antenna in the transverse or yz plane cut, the electric field E_x, its associated phase ψ_{Ex}, and the time-average Poynting vector $\langle \bar{P} \rangle$ are displayed as Fig. 13 to 15. The region mapped is of the same extent and has the same scale, in wavelengths, for the preceding quantities. It is noted that $E_z = 0$, and E_x is all of the main polarization; the cross polarization E_y is vanishingly small. Also, the Poynting vector is composed of P_y and P_z components only, P_x being omitted (intentionally) in the yz cut. In the original plot, which has been photographically reduced here for publication, the maximum computed Poynting vector was limited to L_0 = 3/8-inch on the plot and the minimum value resulting from the calculations was represented as a point or dot. That is,

$$L = \frac{P - P_{min}}{P_{max} - P_{min}} L_0$$

where all power values are taken in decibels. A brief analysis of isophote, wavefront, and power-density plots follows.

Figure 10 also illustrates the region selected for study, above, in addition to tracing the incoming rays through the dual-reflector system. It can be seen that all of the rays converge at a point focus (F) according to the theory of ray optics. In the event that there is no detector at (F), there is a divergent cone of rays in addition to the convergent cone, as shown. It is noted that these rays cross the z-axis at F, the apex of the cones. It is interesting to compare Fig. 10 with Fig. 13 through Fig. 15.and note similarities and differences between ray optics and diffraction theory for the Conical Gregorian system.

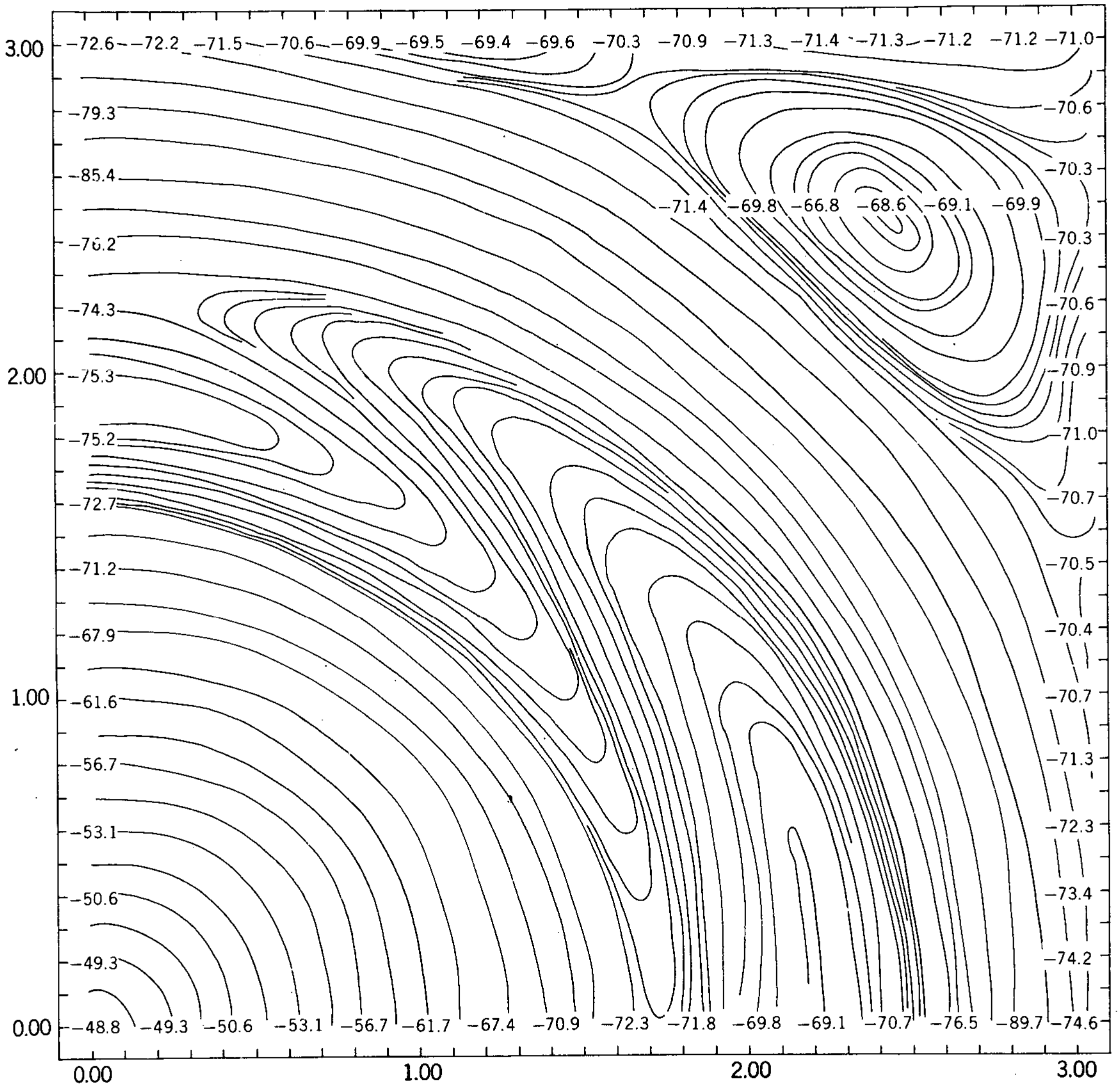

Figure 11. Sector of Airy disc and ring structure $LI_1 = 3.0$ $LI_2 = 1.0$

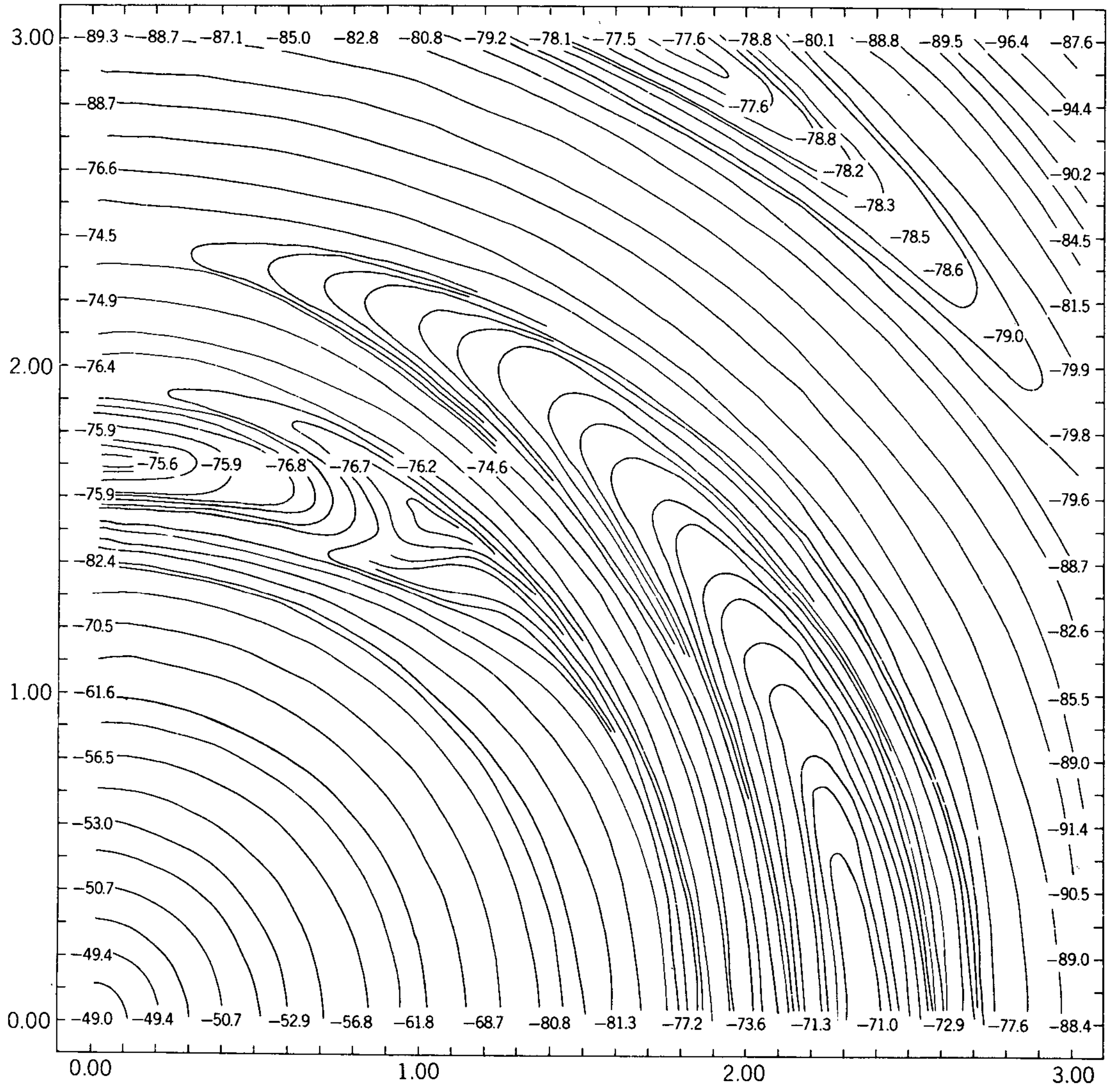

Figure 12. Sector of Airy disc and ring structure $LI_1 = 1.5$ $LI_2 = 0.5$

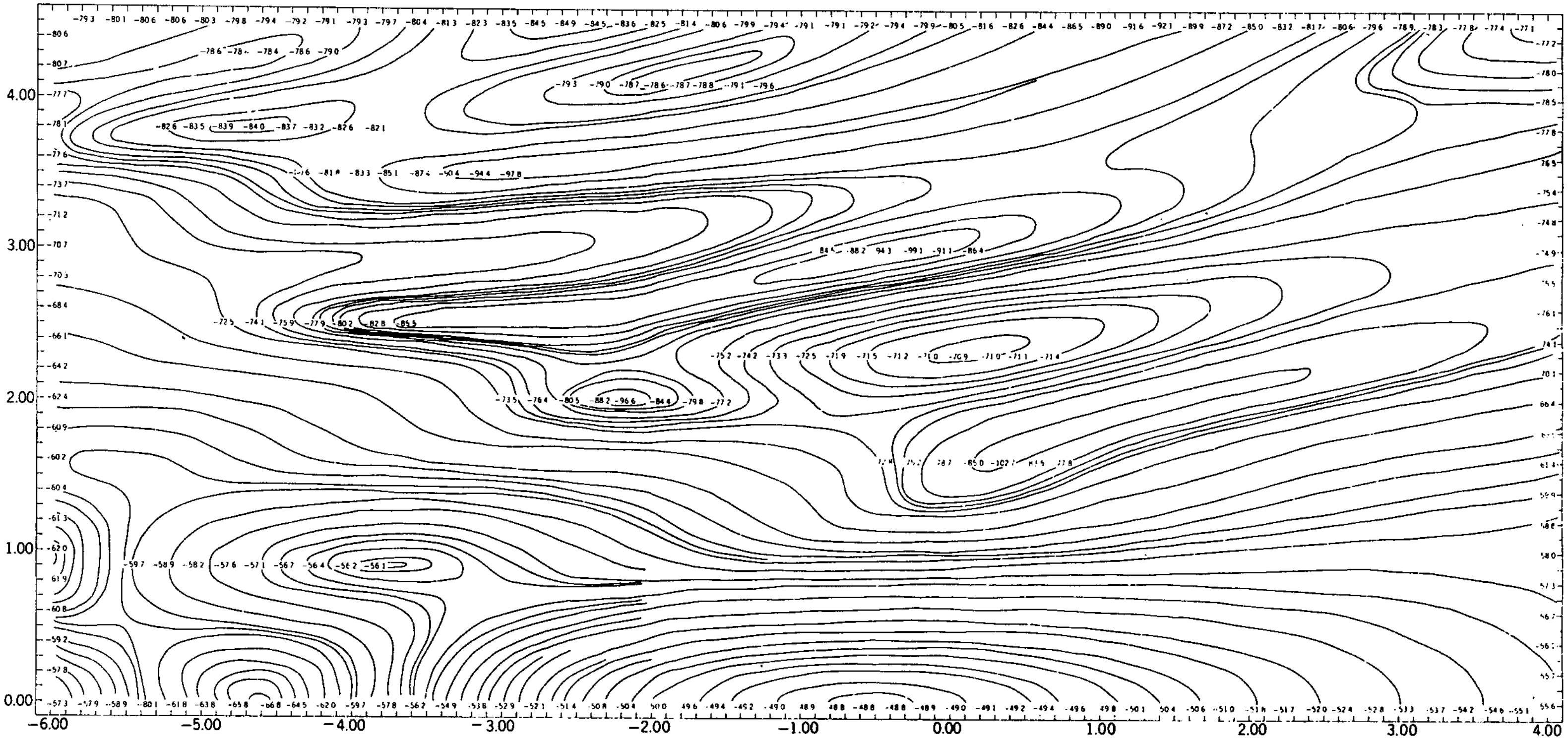

Figure 13. Isophotes E_x in the focal region, $\Delta y = \Delta z = \lambda/10$

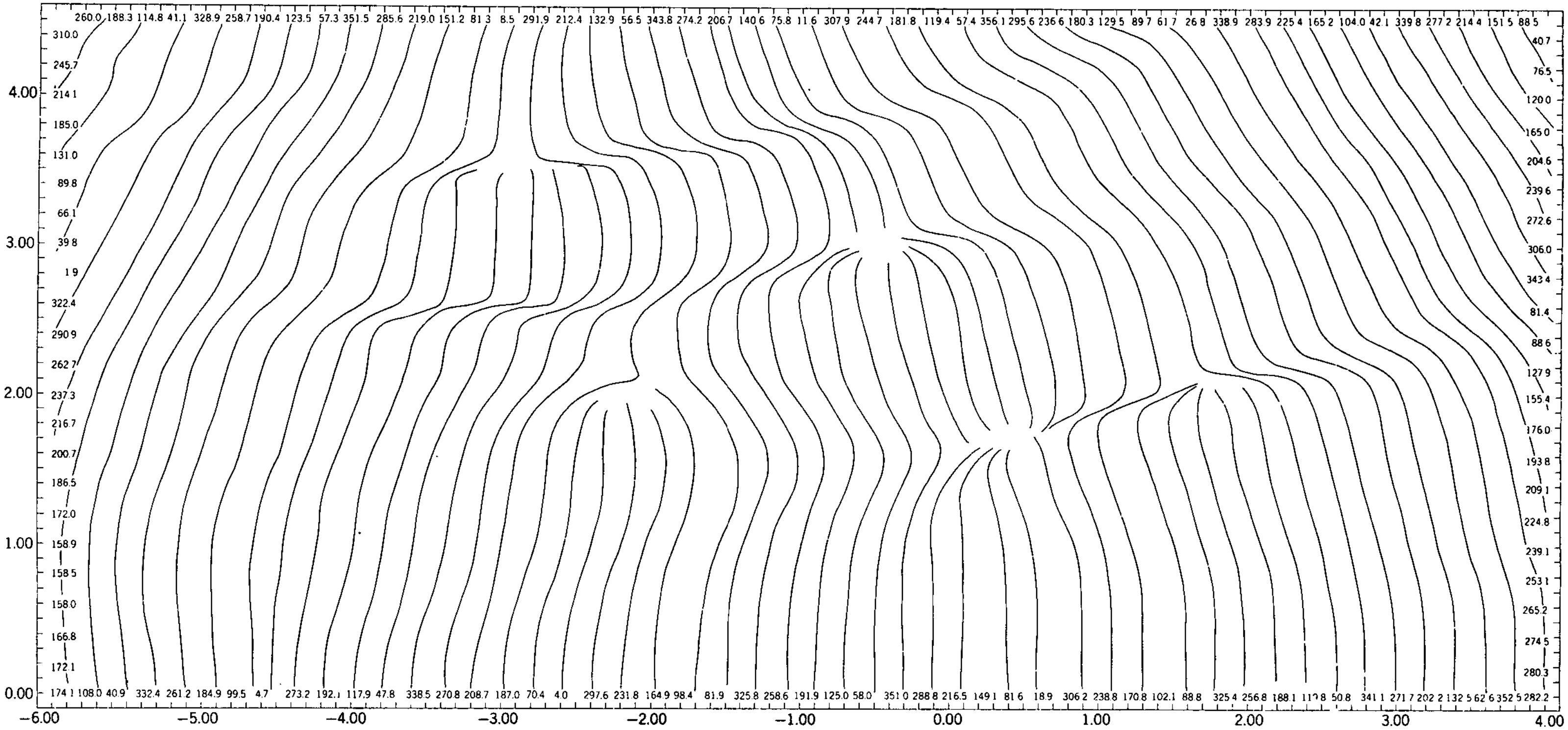

Figure 14. Wavefronts Ψ_{E_x} in the Focal Region, $\Delta y = \Delta z = \lambda/10$

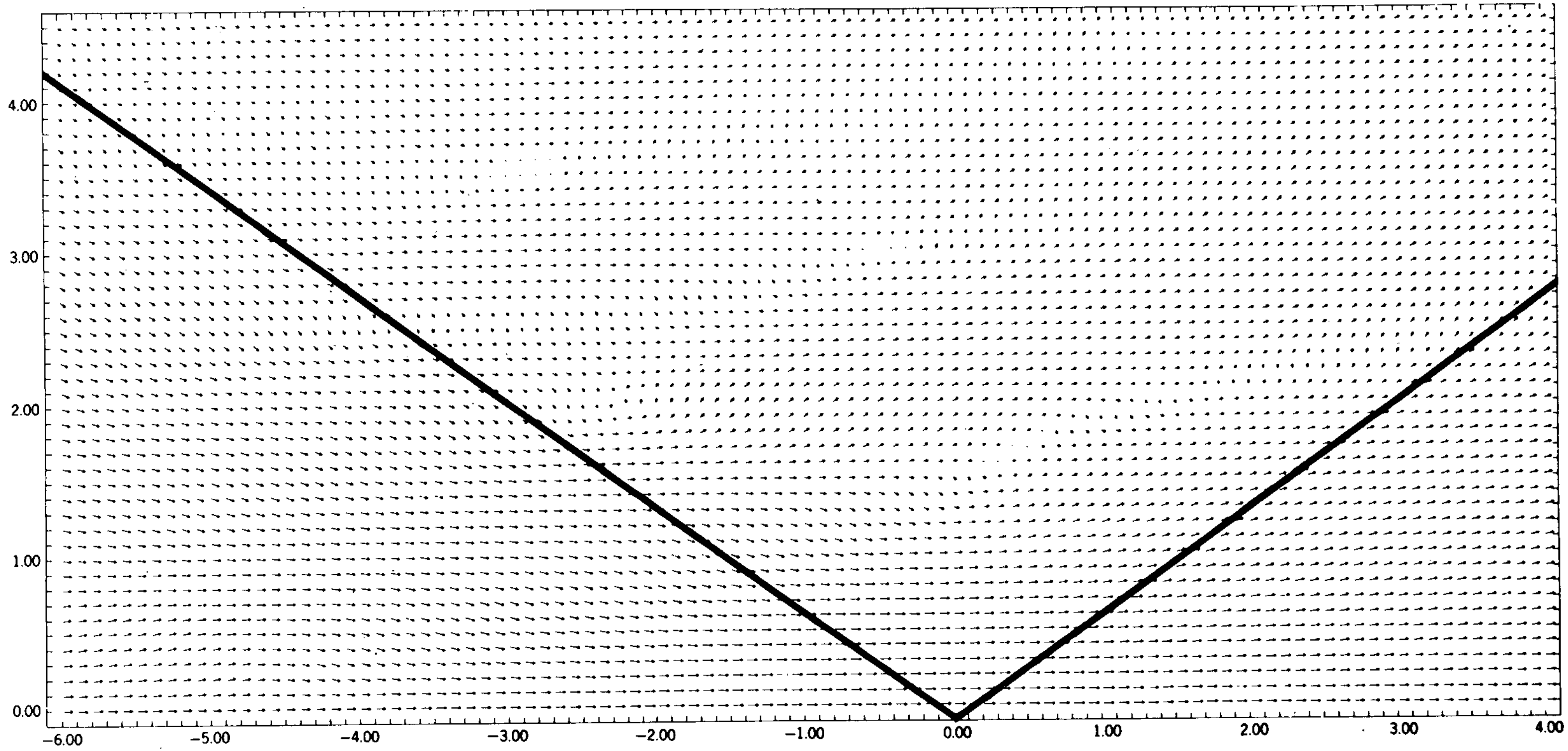

Figure 15. Time-average Poynting vectors in the focal region, $\Delta y = \Delta z = \lambda/10$

Figure 13 shows the constant amplitude contours (isophotes) of the electric field E_x, and provides considerable insight relative to the focussing characteristics of the system. It can be seen that the null-to-null depth of field at this particular frequency, is about 8 wavelengths. The null-to-null width of field is about 3 wavelengths. (The latter can be obtained from Fig. 12, Fig. 13, and Fig. 15.) Even though ray-optics indicates symmetry about the xy plane, diffraction computations show considerable asymmetry at 8.4 GHz. The focal region is distended due to the magnification factor of the system, but is otherwise similar to that of paraboloids.[1]

Figure 14 illustrates the constant phase contours (wavefronts) for the same region depicted by Fig. 13. It can be seen that the perturbed regions of this wavefront plot correspond to the regions where low field intensities (nulls) were observed in Fig. 13. It is possible for the wavefronts of different value (phase) to join at a null field point without contradiction since phase is undefined when amplitude is zero in complex-variable analysis. The wavefront plot should also be compared with Fig. 15, the Poynting vector plot, since the time-average power flow is everywhere orthogonal to the wavefronts. It appears that an increase in phase velocity of about 7 percent is present in the focal region.

Figure 15 shows that the time-average Poynting vectors, $\langle \bar{P} \rangle = 1/2 \, \mathrm{Re} \, \bar{E} \times \bar{H}^*$, obtained via diffraction theory are very different from ray-optics. The geometric bounds shown in this figure are those of the cones of Fig. 10. Power flow tends to conform generally to the prediction of ray optics, but with notable exceptions. For example, the Poynting vectors are bent, or diffracted to pass through the Airy disc and rings without crossing the system axis. Null regions appear in the field, sharp umbral and penumbra regions are everywhere absent, and a vortex-like counterflow of power is observed in the zero-energy isophote regions.

The scaling of the Poynting vectors is such that any noticeable reduction in the length of a vector represents a significant change in the power density at that point. For a dynamic range of 60 db, a reduction of the maximum length of Poynting vector L_0 to $5/6 \; L_0$, $4/6 \; L_0$, $3/6 \; L_0$ corresponds to a reduction in power density of 10 db, 20 db, and 30 db respectively. A careful examination of Fig. 15 shows that very low power densities exist in the umbral region with the exception of those vectors passing through the central portion of the Airy disc. Due to the reduction of Figs. 13 through Fig. 15 from joined Calcomp sheets measuring about 6 feet by 3 feet to the 8-inch by 10-inch document page, it is impossible to extract accurate quantitative data from these reproduced figures. The data field values from which the contours were plotted have been deleted everywhere except around the borders and a few other strategic locations. Photographic reduction would have rendered them unreadable.

---

[1] Ref. 10, pp. 439-449

An enlarged or "magnified" illustration for the region of low intensity near the point (x, y, z) = (3λ, 0, - λ/2) is given as Fig. 16. Here the Poynting vectors, isophotes, and wavefronts are presented in a single sheet to assist the reader in superimposing these features of the electromagnetic fields. Figure 13 through Fig. 15 resolved the field into λ/10 increments. Figure 16 resolves the field into λ/50 increments, and shows an unusual flow of power around a weak isophote that appears to be at least 55 db below the largest field value observed on the system axis at z $\approx$ - λ/2. The phase singularity is seen to coincide with the "null" in intensity.

Further "magnification" of the "null" region was attempted by resolving the field into λ/200 increments. Figure 17 once again shows Poynting vectors, isophotes, and wavefronts. A definite vortex-like counterflow can now be seen for the Poynting vectors. An even weaker isophote, about 85 db below the largest field value can be identified, and the wavefront representation continues to suggest a singularity. The persistence of the counterflow and phase singularity through λ/10, λ/50, λ/200 resolution tends to clarify the fundamental behavior of the electromagnetic characteristics in the vicinity of a null. The results also indicate that the limits of accuracy have not been exceeded with the computer since a high degree of order can be observed in the plots at λ/200 resolution.

SUMMARY

The results obtained in this investigation by means of the GSFC diffraction program agreed closely with measured and computed JPL results for the "Conical Gregorian" configuration. Since JPL Fresnel-region computations were predicated on the use of the spherical-wave expansion method to obtain the illumination distribution on the conical main reflector, it is reasonable to infer the equivalence of the GSFC Huygens-wavelet approach to the expansion method. Although no data are presently available for comparing the computed focal-region fields (isophotes), wavefronts, and time-average Poynting vectors, the results appear valid in terms of the ray-optics predictions. The formulation used herein is, furthermore, the same as that employed with single reflectors (paraboloids) to obtain focal-region information.[1]

Subsequent to the investigation of the Conical Gregorian dual-reflector system, at 8.4 GHz, Ku band 60-foot Cassegrain systems (approaching 1000 λ by 1000 λ) and three-reflector systems have been studied by employing slight variations of the method described herein. It has been found advisable to study

---

[1] Ref. 11

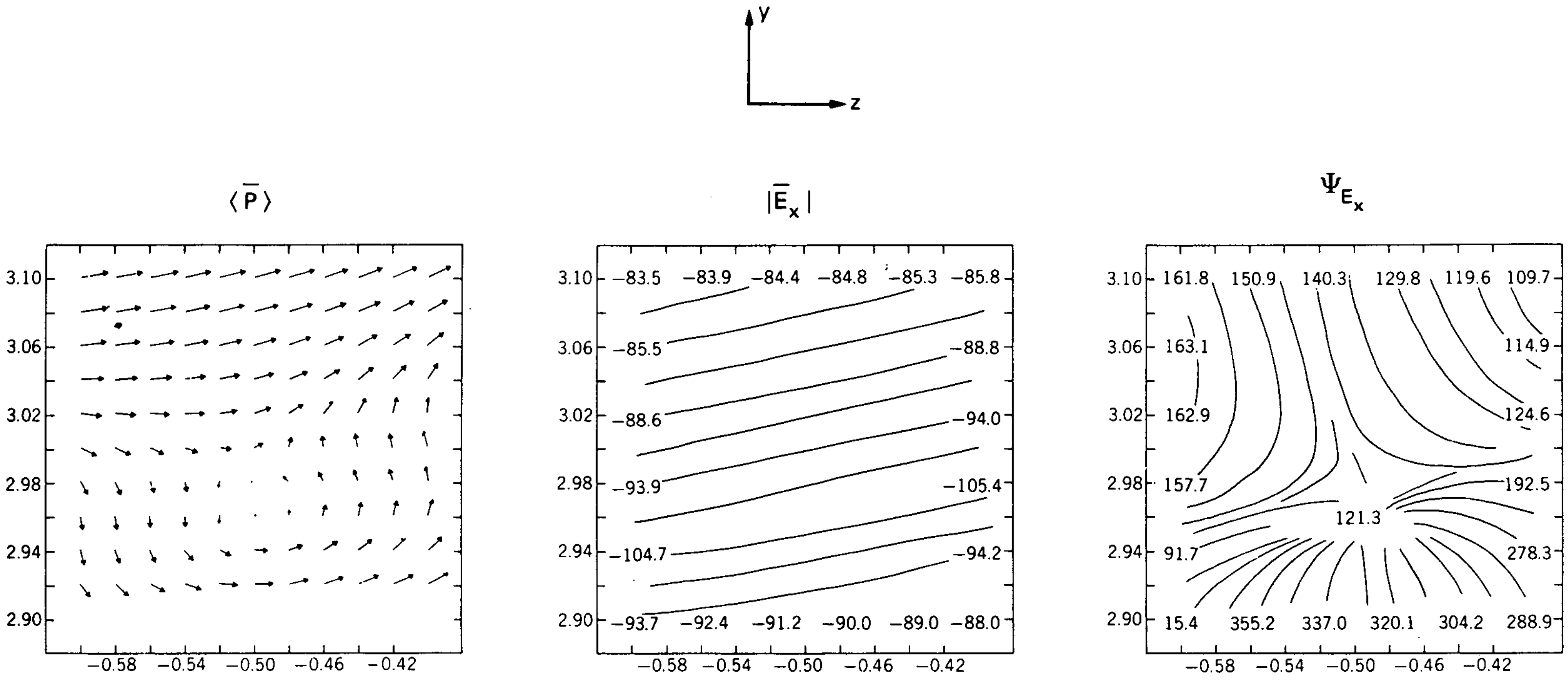

Figure 16. Null-region characteristics, $\Delta y = \Delta z = \lambda/50$

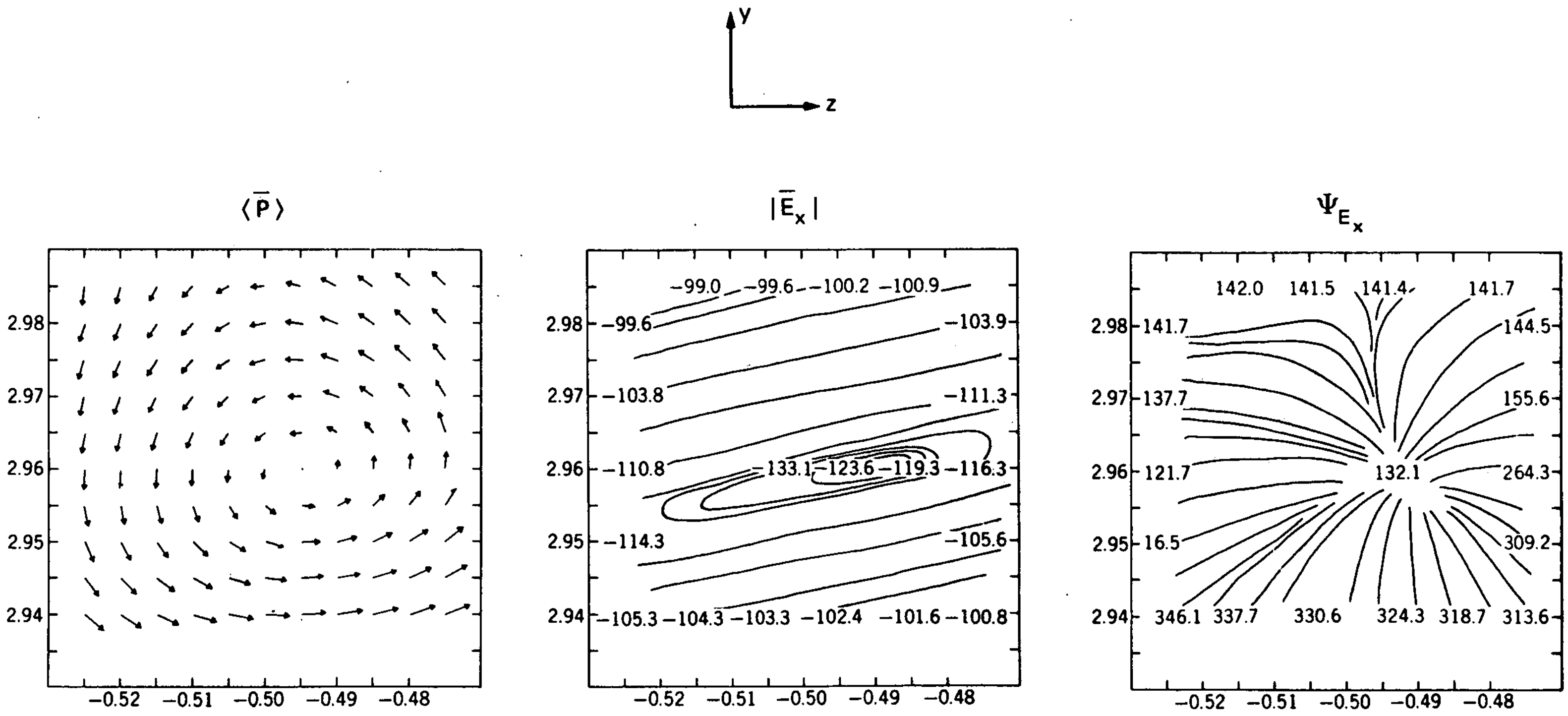

Figure 17. Null-region characteristics, $\Delta y = \Delta z = \lambda/200$

subsystems in detail in the Fresnel region, establish sampling stability (LI), and treat the scattered subsystem fields as prime-feed data. Interpolation is often admissible between a modest number of pattern "cuts" over the subsystem. This approach should be contrasted to the method described in this report, where each charge and current value on a surface is computed by integrating over some other entire surface without any "a priori" knowledge of stationarity on the latter. Symmetry is not assumed with the methods employed in this report.

Present plans call for extensive application of the existing program to ground-based and spacecraft antennas. A number of new subroutines, accommodating unique project geometries and even composite surfaces, are being annexed to the main program. Long-term plans include simulation for electrically-small scatterers ($d < 1\lambda$), artificial dielectrics, and antenna synthesis. This document is an interim report.

ACKNOWLEDGMENTS

The author acknowledges input from the classical literature, periodicals, and journal papers. In particular, the background afforded by Dr. A. C. Ludwig's article, "Conical-Reflector Antennas," in Antennas and Propagation, Volume AP-20, March 1972 is acknowledged, together with discussions with JPL staff personnel. Special recognition goes to Mr. Raymons Miezis and Mr. William Bartley. They developed the (FORTRAN) program used to carry out this study and set up, submitted, retrieved, and plotted the many jobs appearing in the document. Their preliminary efforts, verifications, and unpublished output constitute an even larger contribution.

Mr. Carl Riffe of the Antenna Systems Branch assisted significantly in the development of the parametric representation used for the JPL subreflector. Dr. Sharad Laxpati of the University of Chicago assisted the author, under the auspices of the Faculty Fellowship Program at Goddard Space Flight Center this summer, with valuable commentary and suggestions concerning the near-field aspects of the program. The author is also indebted to Mr. Anthony F. Durham, Branch Head, Antenna Systems Branch, Network Engineering Division for guidance in carrying out this study.

REFERENCES

1. Ludwig, A. C., "Conical Reflector Antennas," IEEE Transactions on Antennas and Propagation, Vol. AP-20, Number 2, March 1972, pp. 146-152.

2. Stratton, J.A., "Electromagnetic Theory," McGraw-Hill Book Company, Inc., 1941.

3. Silver, S. (ed.), "Microwave Antenna Theory and Design," McGraw-Hill Book Company, Inc., 1944.

4. Sancer, M. I., "An Analysis of the Vector Kirchhoff Equations and the Associated Boundary-Line Charge," Radio Science, Vol. 3 (New Series), No. 2, 1968.

5. Tai, Chen-To, "Kirchhoff Theory: Scalar, Vector, or Dyadic?," IEEE Transactions on Antennas and Propagation, January 1972.

6. Franz, W., "Zur Formulierung des Huygensschen Prinzips," Z. Naturforschg., Vol. 3a, July 1948.

7. Farnell, G. W., "Calculated Intensity and Phase Distribution in the Image Space of a Microwave Lens," Canad. J. Phys., 1957, 35.

8. Farnell, G. W., "Measured Phase Distribution in the Image Space of a Microwave Lens, Ibid, 1958.

9. Towne, D. H., "Wave Phenomena," Addison-Wesley Publishing Company, 1967.

10. Born, M. and Wolf, E., "Principles of Optics," Pergammon Press, 1964.

11. Schmidt, R. F., "The Calculation of Electromagnetic Fields in the Fresnel and Fraunhofer Regions using Numerical Integration Methods," X-811-71-392, Goddard Space Flight Center, 1971.

PRECEDING PAGE BLANK NOT FILMED

APPENDIX A

CONICAL MAIN REFLECTOR GEOMETRY

Surface

$$x = \sigma \sin \zeta$$

$$y = -\sigma \cos \zeta$$

$$z = c\sigma + z_1$$

Tangents to Surface

$$\overline{\rho}_\zeta = \frac{\partial \overline{\rho}}{\partial \zeta}, \quad \overline{\rho}_\sigma = \frac{\partial \overline{\rho}}{\partial \sigma}, \quad \overline{\rho} = \hat{i}\, x + \hat{j}\, \hat{y} + \hat{k}\, z$$

Unit Normals to Surface

$$\overline{n} = \frac{\overline{\rho}_\sigma \times \overline{\rho}_\zeta}{|\overline{\rho}_\sigma \times \overline{\rho}_\zeta|} = \frac{\overline{\rho}_\sigma \times \overline{\rho}_\zeta}{(E\,G - F^2)^{1/2}} = \frac{(-c \sin \zeta\, \hat{i} + c \cos \zeta\, \hat{j} + 1\, \hat{k})}{|(1 + c^2)^{1/2}|}$$

Differential Area

$$d\,S = (E\,G - F^2)^{1/2}\, d\sigma\, d\zeta = |\overline{\rho}_\sigma \times \overline{\rho}_\zeta|\, d\sigma\, d\zeta$$

$$E = x_\sigma^2 + y_\sigma^2 + z_\sigma^2 = 1 + c^2$$

$$F = x_\sigma x_\zeta + y_\sigma y_\zeta + z_\sigma z_\zeta = 0 \text{ (orthogonal net)}$$

$$G = x_\zeta^2 + y_\zeta^2 + z_\zeta^2 = \sigma^2$$

$$d\,S = \sigma\,(c^2 + 1)^{1/2}\, d\sigma\, d\zeta$$

Preceding page blank

APPENDIX B

SUBREFLECTOR GEOMETRY

A parabolic arc

$$z'' = x''^2/4F$$

under a rotation transformation

$$T_1:\ z'' = z' \cos\alpha - x' \sin\alpha$$

$$x'' = z' \sin\alpha + x' \cos\alpha$$

about its vertex becomes

$$(z' \cos\alpha - x' \sin\alpha)/4F - (z' \sin\alpha + x' \cos\alpha) = 0.$$

A subsequent translation transformation

$$T_2:\ z' = z + F \cos\alpha$$

$$x' = x - F \sin\alpha$$

which causes the focal point to coincide with the origin of coordinates yields

$$z^2 \sin^2\alpha + z\,(2x \sin\alpha \cos\alpha - 4F \cos\alpha) + (x^2 \cos^2\alpha + 4Fx \sin\alpha - 4F^2) = 0.$$

The quadratic in z then leads to

$$\mathfrak{Z}(x) = z = \frac{(4F\cos\alpha - 2x\sin\alpha\cos\alpha) \pm [(2x\sin\alpha\cos\alpha - 4F\cos\alpha)^2 - 4\sin^2\alpha(x^2\cos^2\alpha + 4Fx\sin\alpha - 4F^2)]^{1/2}}{z\sin^2\alpha}$$

The singularity in the last equation implies the trivial case of rotation for a parabolic arc.

The parabolic arc becomes imaginary when (x) exceeds

$$(2\,x \sin\alpha \cos\alpha - 4\,F \cos\alpha)^2 - 4\sin^2\alpha\,(x^2\cos^2\alpha + 4\,F\,x \sin\alpha - 4\,F^2) = 0$$

or when (x) exceeds

$$x = F/\sin\alpha \qquad (\alpha \neq 0)$$

The corresponding value of (z) is

$$z = F\cos\alpha/\sin^2\alpha \qquad (\alpha \neq 0)$$

Differentiating the solution (z) for the translated and rotated arc with respect to (σ), having let (+ x) → (σ), gives

$$z_\sigma = -\cot \underline{\oplus}\, \frac{[2(2\sigma\sin\alpha\cos\alpha - 4F\cos\alpha)(2\sin\alpha\cos\alpha) - (4\sin^2\alpha)(2\sigma\cos^2\alpha + 4F\sin\alpha)]}{4\sin^2\alpha\,[(2\sigma\sin\alpha\cos\alpha - 4F\cos\alpha)^2 - 4\sin^2\alpha(\sigma^2\cos^2\alpha + 4\sigma F\sin\alpha - 4F^2)]^{1/2}}$$

which reduces to

$$z_\sigma = -\cot\alpha\,\overline{\oplus}\,\frac{1}{\sin\alpha\left(1 - \frac{\sigma}{F}\sin\alpha\right)^{1/2}}$$

The two singularities in the equation, above, have been identified in the preceding discussion.

$$S_1\ @\ \alpha = 0,\ \pi,\ \ldots,\ \pi n$$

implies the trivial rotation, and

$$S_2\ @\ \sigma = \frac{F}{\sin\alpha}$$

implies the imaginary domain for the parabolic arc.

Surface

$$x = \sigma \sin \zeta$$

$$y = -\sigma \cos \zeta$$

$$z = \mathfrak{z}_1 (\sigma) + z_1$$

Tangents to Surface

$$\bar{\rho}_\zeta = \frac{\partial \bar{\rho}}{\partial \zeta}, \quad \bar{\rho}_\sigma = \frac{\partial \bar{\rho}}{\partial \sigma}, \quad \bar{\rho} = \hat{i}\, x + \hat{j}\, y + \hat{k}\, z$$

Unit Normals to Surface

$$\bar{n} = \frac{\bar{\rho}_\sigma \times \bar{\rho}_\zeta}{|\bar{\rho}_\sigma \times \bar{\rho}_\zeta|} = \frac{\bar{\rho}_\sigma \times \bar{\rho}_\zeta}{(E G - F^2)^{1/2}} = \frac{-z_\sigma \sin \zeta\, \hat{i} + z_\sigma \cos \zeta\, \hat{j} + 1\, \hat{k}}{(1 + z_\sigma^2)^{1/2}}$$

Differential Area

$$d S = (E G - F^2)^{1/2}\, d \sigma\, d \zeta = |\bar{\rho}_\sigma \times \bar{\rho}_\zeta|\, d \sigma\, d \zeta$$

$$E = x_\sigma^2 + y_\sigma^2 + z_\sigma^2 = 1 + z_\sigma^2$$

$$F = x_\sigma x_\zeta + y_\sigma y_\zeta + z_\sigma z_\zeta = 0 \quad \text{(orthogonal net)}$$

$$G = x_\zeta^2 + y_\zeta^2 + z_\zeta^2 = \sigma^2$$

$$d S = (E G)^{1/2}\, d \sigma\, d \zeta = \left\{ 1 + \left[-\cot \alpha \,\bar{\oplus}\, \frac{1}{\sin \alpha \left(1 - \frac{\sigma}{F} \sin \alpha \right)^{1/2}} \right]^2 \right\}^{1/2} \sigma\, d\sigma\, d \zeta.$$